Title

Mechanism of Oxidation of Ethane to Ethanol at Iron(IV)–Oxo Sites in Magnesium-Diluted Fe2(dobdc)

Journal

Journal of the American Chemical Society, 137(17)

ISSN

0002-7863

Authors

Verma, Pragya
Vogiatzis, Konstantinos D
Planas, Nora
et al.

Publication Date

2015-05-06

DOI

10.1021/jacs.5b00382

Peer reviewed

JACS
JOURNAL OF THE AMERICAN CHEMICAL SOCIETY
Article
pubs.acs.org/JACS

Mechanism of Oxidation of Ethane to Ethanol at Iron(IV)−Oxo Sites in Magnesium-Diluted Fe_2(dobdc)

Pragya Verma,[†,∥] Konstantinos D. Vogiatzis,[†,∥] Nora Planas,[†,∥,⊥] Joshua Borycz,[†,∥] Dianne J. Xiao,[‡,∥] Jeffrey R. Long,[‡,§,∥] Laura Gagliardi,*[,†,∥] and Donald G. Truhlar*[,†,∥]

[†]Department of Chemistry, Chemical Theory Center, and Supercomputing Institute, University of Minnesota, Minneapolis, Minnesota 55455, United States

[‡]Department of Chemistry, University of California, Berkeley, California 94720, United States

[§]Materials Sciences Division, Lawrence Berkeley Laboratory, Berkeley, California 94720, United States

[∥]Nanoporous Materials Genome Center, University of Minnesota, Minneapolis, Minnesota 55455, United States

[⊥]Department of Chemistry, University of Wisconsin-Eau Claire, Eau Claire, Wisconsin 54702, United States

Supporting Information

ABSTRACT: The catalytic properties of the metal−organic framework Fe_2(dobdc), containing open Fe(II) sites, include hydroxylation of phenol by pure Fe_2(dobdc) and hydroxylation of ethane by its magnesium-diluted analogue, $Fe_{0.1}Mg_{1.9}$(dobdc). In earlier work, the latter reaction was proposed to occur through a redox mechanism involving the generation of an iron(IV)−oxo species, which is an intermediate that is also observed or postulated (depending on the case) in some heme and nonheme enzymes and their model complexes. In the present work, we present a detailed mechanism by which the catalytic material, $Fe_{0.1}Mg_{1.9}$(dobdc), activates the strong C−H bonds of ethane. Kohn−Sham density functional and multireference wave function calculations have been performed to characterize the electronic structure of key species. We show that the catalytic nonheme-Fe hydroxylation of the strong C−H bond of ethane proceeds by a quintet single-state σ-attack pathway after the formation of highly reactive iron−oxo intermediate. The mechanistic pathway involves three key transition states, with the highest activation barrier for the transfer of oxygen from N_2O to the Fe(II) center. The uncatalyzed reaction, where nitrous oxide directly oxidizes ethane to ethanol is found to have an activation barrier of 280 kJ/mol, in contrast to 82 kJ/mol for the slowest step in the iron(IV)−oxo catalytic mechanism. The energetics of the C−H bond activation steps of ethane and methane are also compared. Dehydrogenation and dissociation pathways that can compete with the formation of ethanol were shown to involve higher barriers than the hydroxylation pathway.

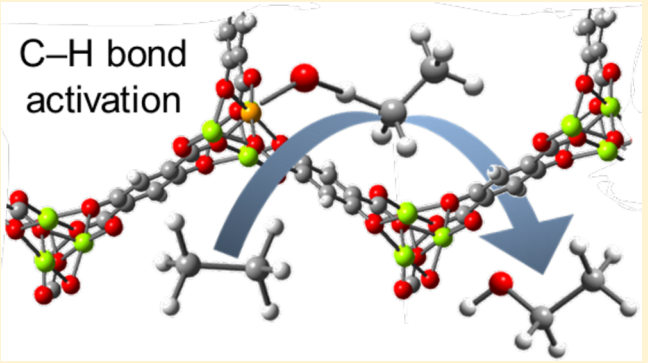

1. INTRODUCTION

The rich chemistry and biology exhibited by high-valent iron−oxo intermediates of heme and nonheme enzymes[1−4] have generated considerable interest. The ability of enzymatic catalysts to oxidize methane to methanol under mild conditions without subsequent further oxidation to CO_2 has inspired a host of synthetic biomimetic catalysts. Much of the synthetic effort has been dedicated toward characterization of synthetic nonheme iron(IV)−oxo intermediates that can activate strong C−H bonds of alkanes and efficiently convert them to useful compounds such as hydroxylated alkanes or alkenes. However, the synthesized mononuclear complexes[5−11] tend to have an S = 1 intermediate-spin (IS)[12−15] iron(IV)−oxo unit, which is in contrast to the enzymatic catalysts, which exhibit a high-spin (HS) ground-state (S = 2) iron(IV)−oxo[16,17,36] unit. Kohn−Sham density functional calculations and simulations[14,18−24] are consistent with most nonheme Fe(IV)−oxo complexes possessing an S = 1 spin state, but with catalysis proceeding on the excited quintet surface that involves a smaller barrier. This has generated interest in designing synthetic materials that have a quintet ground spin state with catalysis proceeding entirely on the quintet surface with an activation barrier that makes the reaction feasible. Two approaches have been used to target such high-spin species, namely: (i) the use of weak-field ligands in an octahedral environment, and (ii) the utilization of ligands that enforce trigonal bipyramidal geometry. An example of the first approach is the compound $[Fe^{IV}O(H_2O)_5]^{2+}$,[7] which has an S = 2 ground spin state and a half-life of only 7 s at 25 °C.[25] Theoretical analyses of this complex indicated that substitution of some of these water molecules by a strong-field ligand can lead to a triplet spin state.[26] This confirms that, as

Received: January 13, 2015
Published: April 17, 2015

DOI: 10.1021/jacs.5b00382
J. Am. Chem. Soc. 2015, 137, 5770−5781

usual, the electron donor properties of ligands surrounding the metal center play an important role in determining the ground spin state. In addition to the ligand donor properties, the geometry of the compound and the sterics of the ligand also play a significant role in determining its spin state. For example, the trigonal bipyramidal iron−oxo complex $[Fe^{IV}(O)(TMG_3tren)]^{2+}$ (TMG_3tren = 1,1,1-tris{2-[N^2-(1,1,3,3-tetramethylguanidino)]ethyl}amine) also has a quintet spin state, as indicated by Mössbauer spectroscopy.[27] However, this complex exhibited reactivity similar to S = 1 iron(IV)−oxo complexes, perhaps owing to the steric bulk of the TMG_3tren ligand that diminishes access to the iron(IV)−oxo unit for oxidation reactions.[28,29]

Metal−organic frameworks (MOFs) with coordinatively unsaturated iron centers surrounded by weak-field oxygen-based ligands are promising scaffolds for accessing high-spin nonheme iron(IV)−oxo intermediates. Here, the porosity of the structure, along with the constraints on the ligand environment imparted by the extended framework, prevent steric hindrance at the iron(IV)−oxo units and provide easy access for reactivity. Recently, it has been shown that oxidation of a MOF with open iron(II) sites by nitrous oxide generates an intermediate, proposed to be a high-spin nonheme iron(IV)−oxo, which can activate the strong C−H bonds of ethane.[30] A theoretical mechanistic investigation of this activation is the focus of the present article.

Previous theoretical mechanistic studies[20,21] on the reactivity of nonheme iron(IV)−oxo intermediates have shown that all three spin states (S = 0, 1, and 2) of the intermediate participate in C−H bond activation. Even if the S = 2 state of the iron(IV)−oxo species is energetically less favorable than the S = 1 state, the S = 2 transition state for C−H bond activation may have a lower energy than the S = 1 transition state. Iron(IV)−oxo complexes exhibiting this behavior can be described as S = 1 reactants with a highly reactive S = 2 spin state.[11] This has been observed for hydroxylation reactions for a series of nonheme model complexes.[20,31] Kohn−Sham studies predict a spin-crossover between the S = 1 and S = 2 states, and the concept of two-state reactivity (TSR) has been used for understanding the mechanism of the reaction.[20,31−34] If the triplet-quintet energy gap of reactants is very small, the triplet ground state may pre-equilibrate with the higher-energy quintet state, and the reaction may proceed on the quintet surface. But if the triplet-quintet gap is larger, the spin-crossover and H-abstraction steps may occur in a concerted fashion. If one makes synthetic materials with weak ligand fields, the quintet state may be lower at both the reactant and the transition-state geometry, and the reaction may occur with single-state reactivity (SSR) on the quintet surface, thereby avoiding the complexity of needing spin inversion.

Once the C−H bond is activated and forms a radical of the substrate, competitive mechanistic pathways can be followed that lead to different products. For example, the hydroxylated product can be formed by an oxygen rebound mechanism, the desaturated product may be formed after another hydrogen atom abstraction, and other possible outcomes can occur due to dissociation of the radical.[35−40] The relative propensity for hydroxylation and desaturation processes is based on two mechanistic scenarios that can be followed after the first hydrogen atom transfer (HAT), which is accompanied by the formation of an Fe(III)−OH intermediate. Rearrangement of the radical-bound Fe(III)−OH intermediate leads to hydroxylation,[3] whereas abstraction of the second hydrogen atom from the substrate radical leads to desaturation.[41] The selection of the preferred pathway is based on electronic and steric inhibition of the rebound of the OH radical,[42] and under controlled conditions, desaturation leading to an olefin can compete with the hydroxylation of an aliphatic C−H bond.[43] It would be interesting to observe the possibility of such a competition in MOFs with Fe(IV)═O units. Hence, we also investigate the three competitive pathways—hydroxylation, desaturation, and dissociation—that have been reported in various cases in the literature, although experimentally only hydroxylation has been observed[30] for the MOF studied here.

Because the intermediates involved in catalytic reactions can be difficult to observe, theory can and has played an important role in elucidating the atomic-level mechanisms of catalytic reactions.[44] Since the instability of synthetic Fe(IV)═O intermediates very often hinders their isolation and crystallographic characterization, Kohn−Sham calculations have played a prominent role in characterizing them, unraveling their properties, and shedding light on their mechanistic details. A lot of activity in this area has led to theoretical concepts that have been shown to be successful in rationalizing the Fe(IV)═O chemistry.[45] The chemistry has been explained within the framework of the following key concepts: (1) SSR vs TSR, which delineates whether a spin change is required to access a surface with a lower activation barrier, (2) the exchange-enhanced reactivity (EER) principle,[46,47] which explains how exchange enhancement[48] of a high-spin pathway promotes its chemical reactivity, while the low-spin pathway will be less favorable due to exchange depletion, and (3) orbital-selection rules, which suggests the preferred geometry adopted by the key transition state for a favorable orbital overlap.

In the present article, we use electronic structure calculations employing both Kohn−Sham density functional theory[49] and multireference wave function theory[50] to study the mechanism of a nonheme iron species that operates as a single-site catalyst supported by a MOF, in particular $Fe_{0.1}Mg_{1.9}$(dobdc), where $dobdc^{4-}$ denotes 2,5-dioxido-1,4-benzenedicarboxylate. This catalyst may also be described as a variant of Mg_2(dobdc) (also known as Mg-MOF-74) in which 5% of the Mg atoms are substituted by Fe. Previous experimental work[30] has shown that, using nitrous oxide (N_2O) as the oxidant, this system can catalyze ethane oxidation with the primary products being ethanol and acetaldehyde. Concomitant theoretical work indicated that the reaction is likely to proceed through a high-spin (quintet) iron(IV)−oxo intermediate. This work extends the iron(IV)−oxo chemistry, that was previously limited mainly to biological systems and their model complexes, to MOFs. Here we elucidate the full mechanism, compare the catalytic cycles for oxidation of ethane and methane, investigate competitive pathways that can compete with the formation of ethanol, and examine the uncatalyzed oxidation of ethane by nitrous oxide (Scheme 1).

The chemical structures used in this study and the computational methods are presented in Section 2 with computational details at the end of the article. Section 3 presents the results and their analyses, and Section 4 summarizes the main conclusions.

2. STRUCTURES AND COMPUTATIONAL METHODS

2.1. Periodic Calculations. A comparison of cell parameters, cell volume, and surface areas for Fe_2(dobdc), Mg_2(dobdc), and $Fe_{0.1}Mg_{1.9}$(dobdc), reported in an earlier work[30] (see Supplementary Table 10 of ref 30) indicates that

DOI: 10.1021/jacs.5b00382
J. Am. Chem. Soc. 2015, 137, 5770−5781

Scheme 1. Three Reactions Investigated in This Work[a]

$$C_2H_5H + N_2O \xrightarrow[75\ ^\circ C]{Fe_{0.1}Mg_{1.9}(dobdc)} C_2H_5OH + N_2 \quad (1)$$

$$CH_3H + N_2O \xrightarrow{Fe_{0.1}Mg_{1.9}(dobdc)} CH_3OH + N_2 \quad (2)$$

$$C_2H_5H + N_2O \xrightarrow{uncatalyzed} C_2H_5OH + N_2 \quad (3)$$

[a]The complete catalytic cycle is studied for reaction (1), the C−H bond activation step is studied for reaction (2) and compared with the same step in reaction (1), and the direct uncatalyzed reaction (3) is also studied and compared to the catalyzed reaction (1).

the catalytic material $Fe_{0.1}Mg_{1.9}(dobdc)$ is closer to $Mg_2(dobdc)$ (shown in Figure 1) than to $Fe_2(dobdc)$. Hence,

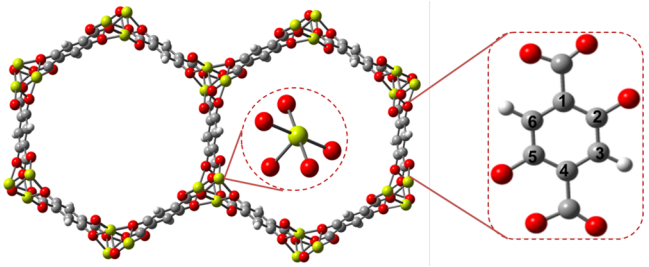

Figure 1. Extended structure of $Mg_2(dobdc)$ (looking down the channels along the crystallographic *c*-axis) shown with its building blocks: pentacoordinate Mg(II) ion and the organic linker, $dobdc^{4-}$ ($dobdc^{4-}$ = 2,5−dioxido-1,4−benzenedicarboxylate). [Color code: light green = Mg, red = O, gray = C, and white = H].

we used the experimetal structure of $Mg_2(dobdc)$ as our starting point to perform periodic Kohn−Sham DFT calculations and model the reaction of interest using a cluster model carved from this periodic structure. The coordinates of the unit cell of the structure resulting from this optimization are given in the Supporting Information.

2.2. Kohn−Sham Cluster Calculations. Because the catalytic reaction under study was observed in a MOF in which Fe is highly diluted by Mg, we assume that catalysis occurs at a single Fe site and does not require Fe−Fe interactions. Therefore, we model $Fe_{0.1}Mg_{1.9}(dobdc)$ by a mixed-metal cluster in which the central metal site is Fe(II) and the other two metal sites are Mg(II); see Figure 2. An 88-atom neutral molecular cluster (with hydrogen atoms included to cap dangling valences and to make the cluster neutral) was carved from the periodic Kohn−Sham optimized structure of $Mg_2(dobdc)$. This cluster has three Mg(II) ions and six organic linkers as shown at the top right of Figure 2, and the central Mg(II) ion was replaced by an Fe(II) ion as shown at the bottom of Figure 2. This mixed-metal cluster was used as the starting structure to determine the reaction intermediates and transition structures. Details of the design of the 88-atom cluster as a model for $M_2(dobdc)$ (also known as M-MOF-74) and its validation have been addressed in previous studies.[30,51]

All Kohn−Sham calculations in the main text were performed with the M06-L[52] exchange−correlation functional using the def2-TZVP[53] all-electron basis set. This basis set has been recommended by Xu et al. for 3d transition metals[54] and

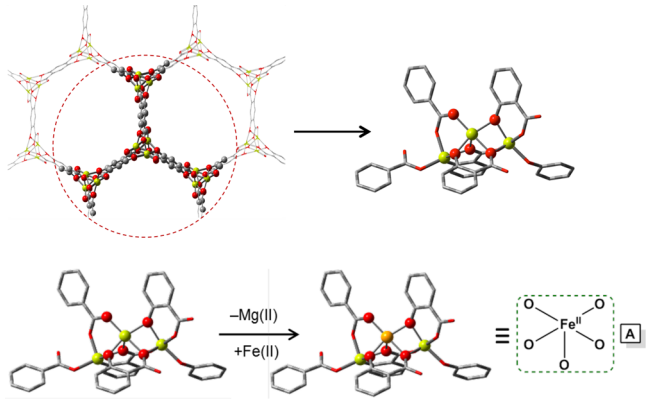

Figure 2. Top: The cluster model of $Mg_2(dobdc)$ carved from its extended structure. The atoms within the dotted circle of the extended structure on the left were truncated to obtain the molecular cluster shown on the right. This cluster has 88 atoms including three Mg(II) ions and six organic linkers. Bottom: The modification of the 88-atom cluster model of $Mg_2(dobdc)$ (left) with three Mg(II) sites to obtain the mixed-metal cluster (center) that is representative of $Fe_{0.1}Mg_{1.9}(dobdc)$ and is used for performing quantum mechanical calculations in this article. The first coordination sphere of this cluster is shown on the right. [Color code: orange = Fe, light green = Mg, red = O, and gray = C]. H atoms are omitted for clarity.

has also been found to provide reasonable results[51] for the separation of hydrocarbons on $Fe_2(dobdc)$ in an earlier work. Since the B3LYP exchange−correlation functional[55] has been widely used to study the Fe(IV)=O chemistry, we did test calculations with it to see how it performs compared to M06-L; these results are shown and discussed in the Supporting Information (see Figures S7 and S8), where the discussion, consistent with previous work,[56−61] indicates that B3LYP is less reliable than M06-L for this problem. Spin densities were calculated from partial atomic charges determined by Charge Model 5 (CM5)[62] using the CM5PAC package[63] with a Hirshfeld population analysis[64] as input. A natural bond order (NBO) analysis[65] was performed for **TS4** as shown in Figure S9 of the Supporting Information.

2.3. Multireference Calculations. Both state-specific (SS) and state-averaged (SA) complete active space self-consistent field[66] (CASSCF) calculations were performed. To make the post-SCF calculations affordable, these calculations were performed on a 26-atom mononuclear model (instead of the 88-atom cluster shown in Figure 2) that contains only the Fe(II) center and the first coordination sphere around it (Figure 3). Validation of the mononuclear model against the 88-atom cluster is reported in Table S5 of the Supporting Information. It should be noted here that all multireference calculations described in this work have been performed with the mononuclear model except for Table S5 where the mononuclear model was validated against the 88-atom cluster. For SA-CASSCF, the molecular orbitals and configuration interaction expansion are equally averaged between the high-spin ground state and the first two, nearly degenerate excited quintet states; each state has a weight of 1/3. For consistency with previous literature[67] and to make a connection with the standard labeling of crystal field theory, the states are labeled by their symmetries in a pure octahedral geometry, even though the actual geometries are distorted with C_1 symmetry. Thus, the ground state at the equilibrium geometry is labeled $^5A_1$, and the

DOI: 10.1021/jacs.5b00382
J. Am. Chem. Soc. 2015, 137, 5770−5781

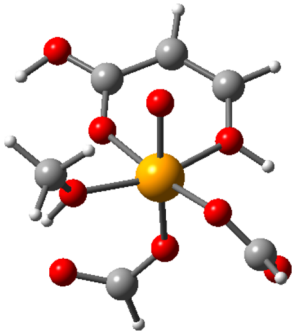

Figure 3. The 26-atom mononuclear model of **B′** used for multireference calculations. [Color code: orange = Fe, red = O, gray = C, and white = H].

next two nearly degenerate states are labeled as ^{5}E(1) and ^{5}E(2).

Multistate second-order perturbation theory[68] (MS-CASPT2) calculations based on the SA-CASSCF reference wave function were performed on two key structures of the catalytic cycle: the iron(IV)−oxo intermediate (this structure will be called **B** in the scheme to be presented below) but without the N_2 (this structure will be called **B′**) and the transition-state structure involving hydrogen atom abstraction from ethane (this structure will be called **TS2** in the scheme to be presented below).

CASSCF calculations were carried out on the mononuclear model of **B′** with an active space of 18 electrons in 12 orbitals and the mononuclear model of **TS2** with an active space of 12 electrons in 11 orbitals. The (18, 12) active space is composed of the three doubly occupied 3p orbitals of Fe, the σ, π_x, π_y bonding and σ^*, π_x^*, π_y^* antibonding molecular orbitals between Fe and O, one 3d nonbonding orbital of Fe ($3d_{xy}$), and a bonding/antibonding orbital pair between the $3d_{x^2-y^2}$ of Fe and the 2p atomic orbitals of the oxygen atoms coordinated to the Fe atom (σ/σ^*). The antibonding counterpart σ^* of this molecular orbital pair is mainly located on Fe. For that reason, it is mentioned in our analysis as $3d_{x^2-y^2}$. Excluding the doubly occupied 3p and the σ^* molecular orbitals of the active space, the electronic structure of the dominant configuration state function (CSF) of **B′** is

$$(\sigma)^2(\pi_x)^2(\pi_y)^2(3d_{xy})^1(3d_{x^2-y^2})^1(\pi_x^*)^1(\pi_y^*)^1(\sigma^*)^0$$

These molecular orbitals define the reactivity of the Fe(IV)═O intermediate, as explained in the next paragraphs and are shown in Figure 5. The remaining four are shown in Figure S1 of the Supporting Information.

An active space of (12, 11) size was used for the mononuclear model of **TS2**. The (12, 11) active space is composed of the four singly occupied 3d orbitals of Fe, three doubly occupied molecular orbitals involving the 2p orbitals of O, two unoccupied 3p orbitals of O and the σ/σ^* molecular orbitals between Fe and the evolving −OH group. The four dominant configurations of **TS2** are given in Table S5 of the Supporting Information.

3. RESULTS AND DISCUSSION

3.1. Catalytic Cycle for the Oxidation of Ethane. The proposed mechanism for the oxidation of ethane to ethanol is shown in Scheme 2. It involves four key steps with four transition-state structures and seven intermediates. The four

Scheme 2. Proposed Mechanism for the Oxidation of Ethane to Ethanol in $Fe_{0.1}Mg_{1.9}(dobdc)$[a]

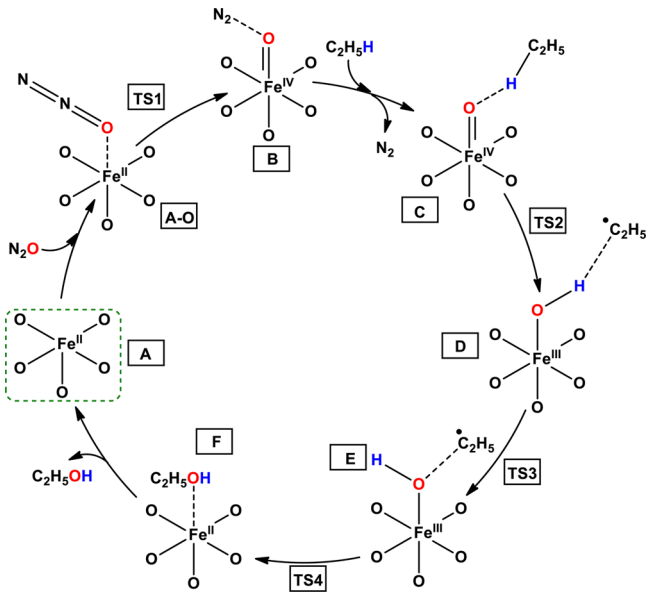

[a]The first coordination sphere of the 88-atom cluster is shown along with the guest species bound to it.

steps are: (1) formation of an iron(IV)−oxo intermediate, (2) C−H bond activation of ethane by the iron(IV)−oxo intermediate, (3) the radical rebound to form ethanol, and (4) the release of ethanol. For every intermediate and transition structure, only the first coordination sphere around the Fe center and the guest molecule bound/reacting with it are shown in Scheme 2. The bare 88-atom mixed-metal cluster is labeled as species **A** (Figure 2). The enthalpy profile of the catalytic cycle is shown in Figure 4. In this profile, the numbers under each energy level correspond to $\Delta H_{298.15}$ (in kJ/mol) calculated with respect to the separated reactants (sum of the

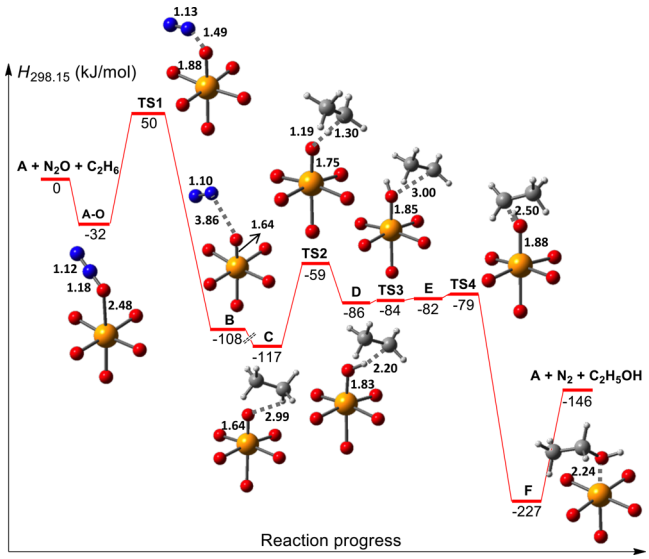

Figure 4. Enthalpy profile, $\Delta H_{298.15}$ (in kJ/mol), calculated relative to reactants (**A** + N_2O + C_2H_6). The first coordination sphere and key bond distances (in Å) obtained by M06-L/def2-TZVP are shown for the intermediates and transition states of the catalytic cycle. [Color code: orange = Fe, red = O, blue = N, gray = C, and white = H].

DOI: 10.1021/jacs.5b00382
J. Am. Chem. Soc. 2015, 137, 5770−5781

energies of bare cluster **A**, N_2O, and C_2H_6). These values are reported for the ground-state geometries of the ground spin state (the results for higher energy conformers and higher energy spin states calculated by performing single-point calculations on the ground-state conformer are shown in Tables S1−S3 of the Supporting Information). The calculated ground spin state for the Fe(II) center is a quintet, for the Fe(III) center it is a sextet, and for the Fe(IV) center it is again a quintet, although the entire complex (intermediate or TS) is always found to be a quintet state owing to the ethyl radical being antiferromagnetically coupled to the Fe(III) center.

It has been very often found in literature that the nonheme Fe(IV)=O model complexes have a triplet ground state, and during C−H bond activation catalyzed reaction the triplet surface crosses the quintet surface.[20,31,32] This crossing occurs in those studies before the rate-determining step (which is usually the C−H bond activation step). It should be emphasized here that, in this work, the rate-determining step is the one that leads to the formation of the Fe(IV)=O intermediate and not the one that involves C−H bond activation (see Figure 4). Our calculations show that the triplet surface is much higher in energy than the quintet surface, and crossing of the two spin surfaces does not occur at any point throughout the whole catalytic cycle (see Table S3 of the Supporting Information). The reaction evolves entirely on the quintet surface. This high-spin state is relatively more stable in the present case than in the nonheme model complexes because the iron centers in the MOF are ligated by the oxygen donor atoms of weak-field ligands. Thus, the catalysis in the present case occurs on a single spin surface, i.e., the present catalyst exhibits SSR.

3.1.1. Iron(IV)−Oxo Formation. The first step of the catalytic oxidation reaction is the adsorption of an N_2O molecule on the uncoordinated Fe(II) site (Scheme 2) of $Fe_{0.1}Mg_{1.9}$(dobdc) (represented by cluster **A**). Structure **A** possesses a high-spin (S = 2) Fe(II) center, with an open site in its first coordination sphere. The S = 2 spin state for Fe_2(dobdc) was verified by magnetic susceptibility measurements performed on the activated framework[69] and by theoretical calculations performed in an earlier work[70] and is confirmed for the mixed Fe/Mg MOF in the current work (see Table S3 of the Supporting Information).

Experimentally it has been found that N_2O binds to **A** yielding two connectivity isomers resulting in the η^1-O (represented by **A−O** in Scheme 2) and the η^1-N (not shown in Scheme 2) coordination modes.[30] A bent Fe−O−N angle in the case of **A−O** and a bent Fe−N−N angle in the case of **A−N**, in both cases ∼120°, are observed from powder neutron diffraction, which was also supported by M06-L and M06[52] calculations in the same work.[30] Both neutron diffraction experiments and Kohn−Sham calculations predict the two binding modes to have similar stabilities. Neutron diffraction experiments predicted the η^1-O coordination to be favored (60%) over the η^1-N coordination (40%),[30] while M06-L calculations of this work predict the η^1-N coordination to be 7 kJ/mol lower in energy than the η^1-O coordination mode.

In the proposed mechanism, the adsorption of N_2O via the η^1-O coordination mode (forming species **A−O**) is followed by the formation of an iron(IV)−oxo intermediate (**B**), which occurs through the cleavage of the N−O bond of N_2O and the subsequent release of N_2 molecule. The transition structure for the release of N_2 to form **B** (**TS1**) has an O−N−N angle of 136° that strongly deviates from the linearity (180°) observed in gaseous N_2O (Figure 4). The activated O−N bond is elongated from 1.18 Å in free N_2O to 1.49 Å in **TS1**.

The complete enthalpy profile is shown in Figure 4. **TS1** is the highest-energy stationary point, and it is associated with the rate-determining step of the reaction; it is found to have an enthalpy of activation of 82 kJ/mol. When this barrier is surpassed, intermediate **B** is reached. This step, that corresponds to the formation of iron(IV)−oxo intermediate, is highly exothermic (ΔH for **A** → **B** is = −108 kJ/mol).

The high-valent iron(IV)−oxo (**B**) is the key intermediate for the activation of the aliphatic C−H bond of ethane. Typically, a weak ligand field or a five-coordinated trigonal bipyramidal ligand field results in a high-spin electronic configuration for the iron center,[2] while stronger field N-donor ligands (e.g., in Fe(II)−porphyrins) favor an intermediate-spin electronic configuration for iron.[71] The high-spin behavior is observed mainly in nature's nonheme cases,[37,12,72] while most of the synthesized nonheme molecular complexes exhibit intermediate-spin ground-state configurations. The coordination sphere around iron in structures **A−O** through **TS4** of Figure 4 (six bonds, five of which are to carboxylate and oxido oxygen atoms of the linker of the MOF) forms a weak-field ligand which allows **B** to be in a quintet state, while, in general, a ligand set of five nitrogen atom bonds and one oxygen atom bond favors an intermediate-spin Fe(IV) configuration.[12] Despite the strong-field ligand character of the oxo unit, the presence of five oxygen atoms that come from the carboxylate and aryloxide groups of the $dobdc^{4-}$ linker enforces a weak ligand field at the Fe center, resulting in **B** being a quintet. The high-spin state is also favored in a series of spectroscopically characterized nonheme iron(IV)−oxo enzymes.[35] In our previous work, CASPT2[73] and M06[52] calculations predicted the energy gap between the high-spin ground state and the intermediate-spin state to be around 130 kJ/mol.[30]

The calculated Fe−O bond distance of 1.64 Å is characteristic of the oxo−ferryl species, indicating a double bond between Fe and O and is in agreement with EXAFS and X-ray diffraction studies on iron(IV)−oxo heme[74] and nonheme enzymes (1.64−1.68 Å).[35] The computed Fe−O stretching frequency of 830 cm^{-1} is within the range of the experimentally observed iron(IV)−oxo frequencies (776−843 cm^{-1}). Intermediate **B′**, which is intermediate **B** without N_2, was further investigated by means of multireference methods, and those results are reported in the next subsection.

3.1.2. C−H Bond Activation. The highly reactive oxo−ferryl group in species **B** interacts with the ethane molecule to form intermediate **C** (shown in Scheme 2). The formation of this intermediate is followed by cleavage of the aliphatic C−H bond of ethane.[20,21] The abstraction of the H atom from ethane (in species **C**) by the iron(IV)−oxo yields a formal iron(III)−hydroxo species with a nearby ethyl radical (referred to as intermediate **D**). This step is accomplished via **TS2**, which has a geometry between the structures of **C** (the reacting ethane bound to iron(IV)−oxo species) and **D**. The Fe−O bond distance is elongated from 1.64 Å in both **B** and **C** to 1.75 Å in **TS2** (Figure 4), while the C−H aliphatic bond is elongated from 1.09 to1.30 Å. The enthalpy of activation for **TS2** is 58 kJ/mol, and its imaginary frequency of 1859i cm^{-1} corresponds to a HAT. **TS2** has a high-spin Fe(III) center (S_{Fe} = 5/2) antiferromagnetically coupled to an unpaired electron of the •O−H−CH_2− group (S_{C-H-O} = 1/2, M_S = −1/2).

DOI: 10.1021/jacs.5b00382
J. Am. Chem. Soc. 2015, 137, 5770−5781

Table 1 shows the energy levels for the different spin states of **TS2**, as calculated by MS-CASPT2 and M06-L. Both methods agree on the $S = 2$ ground spin state and the relative energy of the septet state. The large energy gaps from the septet and triplet states indicate that no spin flip is expected to contribute to the catalytic mechanism.

Table 1. Energy Levels (in kJ/mol) of the Computed Spin States of TS2 Relative to the Quintet State As Reference

spin state	MS-CASPT2[a]	S[c]	M06-L[b]
septet	44	3.0	42
quintet	0	2.1	0
triplet	147	1.3	116
singlet	294	0.7	180

[a]Mononuclear model. [b]88-atom model. [c]Here S represents the spin of the Slater determinant in the M06-L calculation.

It has been shown for the nonheme model compound 1,1,1-tris{2-[N^2-(1,1,3,3-tetramethylguanidino)]ethyl}amine) Fe^{IV}=O that competing σ- and π-electrophilic attacks lead to catalytic reactivity and self-decay channels, respectively;[67] both involve a hydrogen abstraction, either from the substrate or from ligand C−H bonds, respectively. Similarly, in the $Fe_{0.1}Mg_{1.9}$(dobdc) environment, the σ- and π-pathways are in principle both available for ethane activation; the orientations of the σ, σ^*, π, and π^* molecular orbitals (shown in Figure 5) allow both scenarios. The higher probability of one pathway over the other is determined by the geometry and electronic structure of **TS2**, in particular by the bonding behavior between the formerly iron(IV)−oxo species and the developing −OH group arising due to the activation of C−H bond.

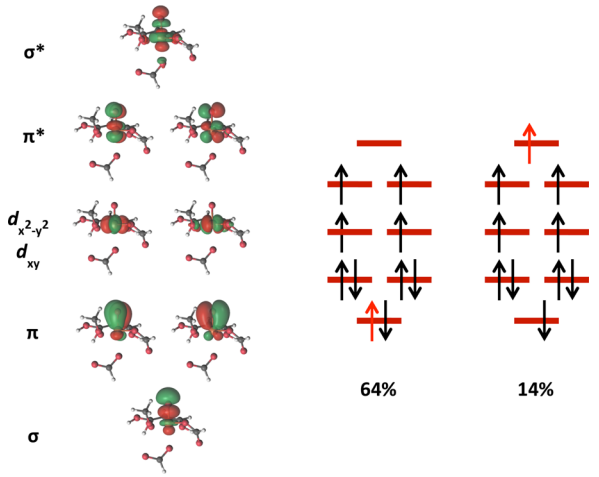

Figure 5. (Left) SA-CASSCF natural orbitals of iron(IV)−oxo for the mononuclear model of structure **B′**. (Right) The electronic occupation and weights of the two leading configurations of the configuration interaction expansion for the $^5A_1$ ground state, as obtained from SA-CASSCF calculations. The ordering of the orbital levels on the right is the same as the ordering of the orbitals on the left. The 3p orbital and ligand molecular orbitals of the active space are not shown. The red arrow corresponds to the electron of the $\sigma \rightarrow \sigma^*$ transition.

As explained in detail in the Supporting Information (Figure S2), the existence of avoided crossings of ^{5}E-like states with the $^5A_1$ state at an Fe−O distance of about 1.85 Å indicates that both σ- and π-channels are accessible if enough energy is available, but the σ-channel should dominate under thermal conditions. The reason for this is clear by examination of Figure 5, which shows the molecular orbitals and the two leading configurations in the SA-CASSCF treatment of the mononuclear model of structure **B′**. The first configuration (64%) is not reactive. The 2p orbitals of the oxo group are doubly occupied, and they cannot activate the C−H bond. Upon increase of the Fe−O distance, the weight of the second, reactive electronic configuration is increased. In the configuration involving $\sigma \rightarrow \sigma^*$ excitation, the σ orbital is singly occupied; this MO is mainly located on the O atom, and it is the orbital that reacts with the C−H bond of the ethane (σ-mechanism). At an Fe−O distance of 1.70 Å, which is the Fe−O distance at **TS2**, the σ MO is purely a $2p_z$ orbital. In the ^{5}E-like excited states, the $2p_x/2p_y$ orbitals of the O atom are singly occupied, and they enable the π-mechanism.

The relative energies of the σ- and π-mechanisms were examined by CASPT2. Two mononuclear models were formed for the σ- and π-mechanisms, respectively, based on the DFT optimized geometry of **TS2**. Further discussion on the electronic structure of the two models is provided in the Supporting Information. The model structure that involves hydrogen abstraction via the σ-channel is more stable by 24.3 kJ/mol than the π-channel structure. We conclude that the π-mechanism is energetically less favorable than the σ-mechanism but thermally accessible for the C−H bond activation of ethane at the Fe(II) site of $Fe_{0.1}Mg_{1.9}$(dobdc). This finding is in agreement with computational studies on nonheme Fe(IV)−oxo complexes.[75,76]

3.1.3. Formation of Ethanol. This step involves the reaction of the iron(III)−hydroxo complex with the ethyl radical to form ethanol. Intermediate **D** undergoes conformational change via **TS3** to give intermediate **E**. The ethyl radical in intermediate **E** abstracts the hydroxyl group bound to the Fe(III) site to form ethanol. This step is usually called the rebound mechanism in the literature, and it involves **TS4**, which has a significantly lower enthalpy of activation (3 kJ/mol) than **TS1** (82 kJ/mol) and **TS2** (58 kJ/mol). For **TS4**, the (alkyl)C···O(hydroxyl) distance is 2.50 Å (Figure 4), in agreement with similar Fe(OH)···$CH_2^{\bullet}$−R transition states (2.33−2.82 Å) reported in literature.[20] We carried out an NBO analysis (Figure S9 of the Supporting Information), which shows that **TS4** has a high-spin Fe(III) center ($S_{Fe} = 5/2$) antiferromagnetically coupled to the ethyl radical ($S_C = 1/2$, $M_S = -1/2$) through the hydroxyl group. The five α electrons of Fe(III) are coupled with the antiparallel electron of the ethyl radical via the doubly occupied oxygen 2p orbital of the hydroxyl group. The presence of a β electron on the carbon of the ethyl radical has also been verified by Hirshfeld population analysis.

The formation of **TS4** is preceded by (1) a rotation of hydrogen atom of the hydroxo group along the Fe(III)−O axis in intermediate **D** that leads to intermediate **E** via **TS3** and (2) a shift of the ethyl radical toward the Fe(III)−OH center. The first circumvents the stereochemical hindrance from the hydrogen atom of the hydroxyl group. The second allows the ethyl radical to approach the hydroxyl group in such a manner that the C−O bond formation (that ultimately results in the generation of ethanol) is favored. In **TS2**, the O−H−C−C torsional angle in the complex (where H−C−C comes from the ethyl radical) is about 180° (Figure 4), while the same torsional angle for **TS4** is about 105°. This favorable angle enables the formation of ethanol from **TS4** and recovery of the Fe(II) active site (intermediate **F**). As has been suggested by Usharani

DOI: 10.1021/jacs.5b00382
J. Am. Chem. Soc. 2015, 137, 5770−5781

Table 2. CM5 Charges (in atomic units), Hirshfeld Spin Densities (in atomic units), and Distances (in Å) Computed for Various Species

species	A	A−O	TS1	B	C	TS2	D	TS3	E	TS4	F
oxidation state	II	II	III	IV	IV	III	III	III	III	III	II
Fe spin density	3.65	3.64	3.89	3.33	3.33	3.86	4.04	4.04	4.04	3.99	3.65
O6 spin density	NA[a]	0.01	−0.06	0.51	0.51	0.13	0.31	0.33	0.33	0.26	0.03
charge on Fe	0.71	0.67	0.85	0.87	0.88	0.88	0.88	0.87	0.87	0.85	0.67
charge on O6	NA[a]	−0.04	−0.29	−0.47	−0.45	−0.53	−0.63	−0.62	−0.62	−0.60	−0.42
⟨charge on O1−5⟩[b]	−0.41	−0.41	−0.41	−0.40	−0.40	−0.40	−0.40	−0.40	−0.40	−0.40	−0.41
Fe−O6 distance[c]	NA[b]	2.48	1.88	1.64	1.64	1.75	1.83	1.85	1.85	1.88	2.24
⟨Fe−O distance⟩[d]	2.08	2.08	2.10	2.12	2.12	2.13	2.13	2.12	2.12	2.13	2.10

[a]Intermediate **A** is the bare cluster and does not have an oxygen bound at its sixth site. [b]Average charge on the five MOF oxygen atoms in the first coordination shell of Fe. [c]O6 is the oxygen atom transferred from N_2O to the iron center. [d]Average Fe−O distance for the five MOF oxygen atoms in the first coordination shell of Fe.

et al.[77] and Ye et al.,[78] a σ-mechanism for hydrogen abstraction is followed by a π-rebound mechanism, i.e., an electron transfer from the singly occupied MO of the ethyl radical to the $3d_{xz/yz}$ orbital of Fe(III) occurs. Similarly, a π-mechanism for hydrogen abstraction will be followed by a σ-rebound mechanism (electron transfer from the ethyl radical to the $3d_{x^2-y^2}$ orbital of Fe(III)). These mixed σ/π and π/σ pathways are based on the overlap of the electron-donating and electron-accepting orbitals. Thus, since the σ-rebound mechanism is calculated here to be energetically more favorable, an electron transfer from the 2p orbital of the oxygen to the $3d_{xz/yz}$ orbital of Fe(III) is expected. An electron de-excitation from the $3d_{xz/yz}$ to the $3d_{xy}$ orbital forms the Fe(II) center of intermediate **F**. Simultaneously, in intermediate **E**, the singly occupied 2p orbital of the oxygen can overlap with the 2p of the carbon from the ethyl radical and form the C−O bond of ethanol.

Figure 4 summarized the reaction steps of the oxidation of ethane to ethanol. The complete reaction profile with the first coordination sphere of Fe for each intermediate and transition state are included. The overall reaction is exothermic by 146 kJ/mol.

Table 2 includes selected parameters monitored for the electronic structures of the intermediates and transition states along this reaction path for the Fe center and the six oxygen atoms around it (shown in Figure 6). The Hirshfeld spin

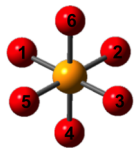

Figure 6. First coordination sphere around Fe for all the species except **A**. Atoms O1−O5 are the five MOF oxygen atoms around the Fe center, and O6 is the oxygen atom transferred from N_2O to the iron center. [Color code: Orange = Fe and red = O].

density on the iron center for various intermediates and transition states lies between 3.33 and 4.04, indicating high-spin states. The CM5 charge on the iron center of the bare cluster (**A**) is 0.71 atomic units and of **A**−**O** is 0.67 atomic units, indicating that the adsorption of N_2O is accompanied by the transfer of positive charge from iron to the rest of the atoms of the complex. These charges are smaller than that of the iron center of most of the species (**TS1**, **B**, **C**, **TS2**, **D**, **TS3**, **E**, and **TS4**). This can be attributed to the O6 atom (that was initially part of N_2O) being closer to the iron center in these species than in intermediates **A**, **A**−**O**, and **F**. The increase in positive charge of the iron center as one goes from **A**−**O** to **TS4** is also reflected in the increase in negative charge of O6 as the reaction progresses. However, the average charge on the five oxygen atoms (O1−O5) coordinated to Fe remains almost unchanged during the catalytic cycle, indicating no incipient oxidation/reduction of the oxygen atoms ligated to the iron center.

Similarly, the average Fe−On (n = 1−5) bond distances show negligible variation as one goes along the reaction path and as the nature of the catalytic site varies. After surmounting the energy barrier of **TS1**, the iron(II) center of intermediate **A**−**O** shifts to oxidation state IV of the highly reactive oxy−ferryl. In parallel, the spin density on Fe is reduced from 3.64 (**A**−**O**) to 3.33 (**B** & **C**). This is also accompanied by increase in spin density on O6 from 0.01 to 0.51. The formation of the iron(III)−hydroxo group (in **D**, **E**, and **TS3**) increases the spin density of Fe, before returning to the initial coordinatively unsaturated species (**A**). The evolution of the bond distance from Fe to the reactive oxygen (O6) is shown in Table 2. The Fe−O6 distance varies from 2.48 Å in **A**−**O** (when N_2O is adsorbed), reaches a minimum of 1.64 Å for species **B** and **C** (the iron(IV)−oxo species), and finally increases to 2.24 Å (**F**) before the release of the ethanol product.

3.2. Comparison of the C−H Bond Activation Step for Methane and Ethane. In contrast to the hydroxylation of ethane, the oxidation of methane by nitrous oxide on the coordinatively unsaturated Fe sites of $Fe_{0.1}Mg_{1.9}$(dobdc) has not yet been found to occur under similar reaction conditions.[30] The goal of the work presented in this subsection is to understand why the reaction for ethane is feasible on the surface of $Fe_{0.1}Mg_{1.9}$(dobdc), while that for methane is much more difficult. The conventional starting point for such a discussion is to compare bond energies; the experimental bond dissociation enthalpies at 298 K are 439 kJ/mol for methane and 423 kJ/mol for ethane,[79] indicating that the C−H bond of methane is stronger than that of ethane by 16 kJ/mol. For comparison, we note that M06-L (with scaled frequencies as explained below in Section 5, Computational Details) gives 432, 409, and 23 kJ/mol for these quantities, in good agreement with experiment. With this background, we studied the energetics of the C−H bond activation step of reactions 1 and 2 (Scheme 1).

Figure 7 shows the reaction profiles for the hydrogen abstraction step of methane (red) and ethane (black). This step involves intermediates **C** and **D** and **TS2**. The enthalpies for both the reactions are reported under the energy levels. We find that the formation of **D** is more exothermic for ethane than for methane, hence the methyl radical intermediate **D** is energeti-

DOI: 10.1021/jacs.5b00382
J. Am. Chem. Soc. 2015, 137, 5770−5781

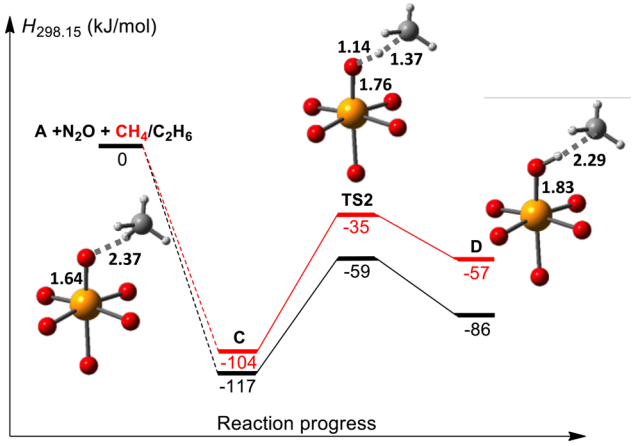

Figure 7. Comparison of enthalpies associated with the C−H bond activation step for CH_4 (red) and C_2H_6 (black) obtained by M06-L/def2-TZVP. The first coordination sphere of Fe for the intermediates **C** and **D** and **TS2** of the CH_4 cycle are shown with key bond distances in Å. The dotted lines in the enthalpy profile indicate that the reaction does not go directly from the reactants (**A** + N_2O + CH_4/C_2H_6) to intermediate **C**. [Color code: orange = Fe, red = O, gray = C, and white = H].

cally less favorable than the ethyl radical intermediate **D**. The difference is 29 kJ/mol, similar to 23 kJ/mol calculated bond enthalpy difference mentioned in the previous paragraph. The enthalpy of activation from **C** to **TS2** for ethane is 58 kJ/mol, while for methane it is 69 kJ/mol, a difference of 11 kJ/mol. Thus, the calculations predict that 38% of the 29 kJ/mol reaction energy difference shows up in the enthalpy of activation, and consequently activation by iron(IV)−oxo is more facile for ethane than for methane. The 11 kJ/mol difference is smaller than the reliability of the theoretical methods for absolute barrier energies, but we believe it is well within the reliability of the method we used for relative energy differences of two similar processes. This can be illustrated by an example. The mean unsigned error in the M06-L values for the electronic binding energies (including nuclear repulsion but excluding vibrational contributions) of H and CH_3 to C_2H_5 is 14.5 kJ/mol, but M06-L reproduces the difference of these energies within 0.2 kJ/mol (predicting 54.3 kJ/mol vs an accurate value of 54.5 kJ/mol); this illustrates how relative energies are often more accurate than absolute energies.

Figures 4 and 7 also show key bond distances for ethane and methane, respectively. For both the cycles, the Fe−O distances (here O is the terminal oxygen atom that is transferred from N_2O to Fe(II)) of **C** and **D** and **TS2** remain the same to within 0.01 Å, but there are larger differences in bond distances of the partial bonds to the transferred H. In particular, we find a shorter O−H distance (1.14 Å) of the **TS2** optimized geometry of methane catalytic cycle compared to ethane catalytic cycle (1.19 Å), and simultaneously the distance between the activated hydrogen atom and the methyl radical is 1.37 Å, which is 0.07 Å longer than the hydrogen−ethyl radical distance. These two trends suggest that the **TS2** structure for methane has more product-like iron(III)−hydroxo character than the **TS2** structure for ethane, which is consistent with the Hammond postulate[80] since the methane reaction is endothermic with a higher barrier. The methyl radical of intermediate **D** lies 2.29 Å away from the hydroxyl group, which is 0.09 Å longer compared to that of the ethyl radical of **D** (2.20 Å). Therefore, for both **TS2** and **D**, the methyl radical is farther away from the evolving −OH group, and it destabilizes the C−H activation mechanism in comparison to the C−H activation of ethane.

The step from **C** to **TS2** has an activation enthalpy of 69 kJ/mol for methane, as compared to 58 kJ/mol for ethane, which—other things being equal—would make this step slower for methane by a factor of 85 at 298 K.

3.3. Competitive Pathways After the Formation of Intermediate D. Since various pathways can be followed after an alkyl radical is formed from an alkane, we computed two competitive pathways, namely desaturation and dissociation, that can in principle compete with the hydroxylated product that is usually formed upon C−H bond activation by nonheme model complexes after the formation of intermediate **D**, as shown in Scheme 3. Desaturation would involve the abstraction

Scheme 3. Competitive Pathways That Can Follow after the Formation of the Ethyl Radical in Intermediate D

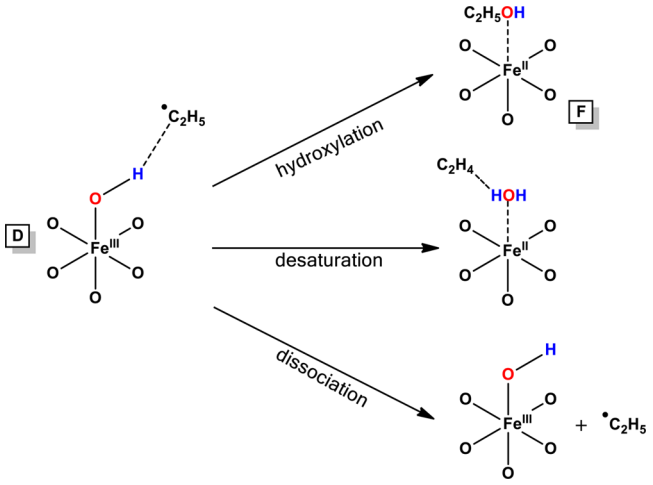

of H atom from ethyl radical to form ethylene and water, and dissociation would involve the departure of ethyl radical without undergoing rebound. The departed ethyl radical can react with other reagents in its vicinity and give rise to secondary products. A comparison of enthalpies of activation associated with hydroxylation and desaturation pathways is shown in Figure 8. It can be seen from Figure 8 that hydroxylation and desaturation pathways have enthalpies of activation of 7 and 27 kJ/mol, respectively, indicating that hydroxylation is more facile than desaturation by 20 kJ/mol. The dissociation of the ethyl radical from intermediate **D**

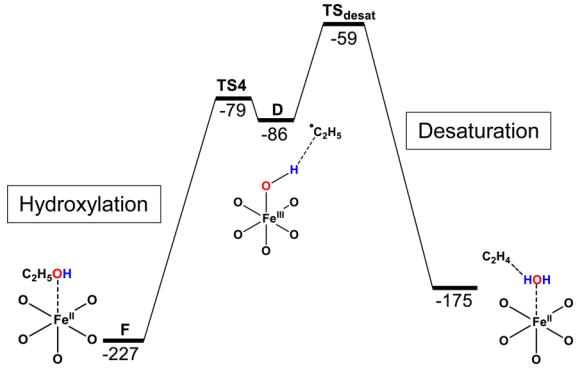

Figure 8. $\Delta H_{298.15}$ (kJ/mol) computed with respect to the separated reactants (cluster **A** + N_2O + C_2H_6) using M06-L/def2-TZVP.

DOI: 10.1021/jacs.5b00382
J. Am. Chem. Soc. 2015, 137, 5770−5781

required 21 kJ/mol, which is again three times more than the enthalpy of activation for hydroxylation. The dissociation of the methyl radical from the corresponding intermediate **D** (shown in Figure 7) required 14 kJ/mol. Since this is smaller than for the ethyl radical dissociation, the rebound to produce methanol is less likely to occur than the rebound that produces ethanol.

The energy diagram of Figure 8 shows that the desaturation process is both kinetically and thermodynamically less favorable than hydroxylation. The Fe(III)−OH group of intermediate **D** is directed toward the inside of the pore of the material, and it can be approached without steric hindrance by both the carbon and the hydrogen atoms of the ethyl radical, which can lead to hydroxylated and desaturated products, respectively. Usharani et al.[77] have shown that the probability of the desaturation reaction depends on the energy gap between the doubly occupied σ_{C-H} orbital and the singly occupied φ_C orbital of the alkyl radical. For the ethyl radical, they calculated this gap to be ∼560 kJ/mol, which was relatively large in comparison to other substrate radicals (377−427 kJ/mol) formed from cyclic hydrocarbons investigated in the same work; the largeness of this value explained why the hydroxylation pathway is preferred. Similar analysis for the free ethyl radical in the present work, using M06-L, gives ∼542 kJ/mol for the same orbital energy gap, again indicating that hydroxylation is the preferred pathway.

3.4. Comparison of Catalyzed and Uncatalyzed Reactions. Finally, the reaction between ethane and nitrous oxide in the absence of any catalytic material was examined. This gives us an estimate of the reduction in energy barrier that is achieved due to the catalyst. To investigate this, the direct hydroxylation of ethane by nitrous oxide was studied, where the reaction is not facilitated by an iron(IV)−oxo intermediate supported by the catalytic material (eq (3), Scheme 1). Figure 9 shows the enthalpy associated with the uncatalyzed reaction process. The enthalpy of activation for this direct step is considerably higher (280 kJ/mol) than the highest enthalpy of activation of the catalyzed reaction (82 kJ/mol), indicating that the direct pathway is highly unfavorable. We find that this direct pathway occurs without the formation of an ethyl radical, which differs from what is observed for the catalyzed reaction. This is confirmed by following the minimum energy path[81] from the saddle point; this path leads to the reactant and product (**A** and **B**, respectively) shown in Figure 9. Unlike the catalyzed reaction, this one-step reaction involves the simultaneous cleavage of the C−H and N−O bonds and the rearrangement of the −OH group to give ethanol directly without proceeding via the formation of an intermediate containing ethyl radical. The transition state of Figure 9 explains this mechanism; both C−H and N−O bonds are activated before the insertion of oxygen in the developing ethyl radical. This reaction profile has also been investigated using a number of other density functionals, and more results are given in the Supporting Information in Table S7.

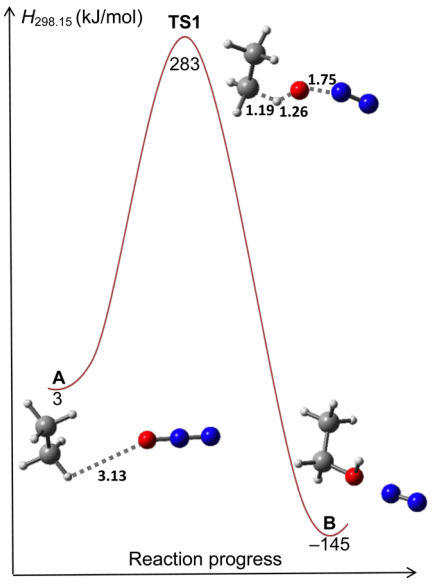

Figure 9. Enthalpy profile, $\Delta H_{298.15}$ (kJ/mol), relative to reactants, for the uncatalyzed reaction (eq 3, Scheme 1) using M06-L/def2-TZVP with key distances in Å. [Color code: red = O, blue = N, gray = C, and white = H].

4. CONCLUSIONS

The ability of the magnesium-diluted MOF, $Fe_{0.1}Mg_{1.9}$(dobdc), to catalyze the oxidation of ethane in the presence of N_2O has been studied. This reaction was originally suggested[30] to proceed via the formation of a high-spin S = 2 iron(IV)−oxo intermediate, and here we elucidate the full mechanism. An 88-atom cluster model carved from a periodic Kohn−Sham optimized geometry of Mg_2(dobdc) was used for the Kohn−Sham cluster calculations to locate the stationary points, two of which were further analyzed by multireference calculations and NBO analysis using a smaller cluster. We showed that the metal−organic framework catalyzed hydroxylation of ethane proceeds by an S = 2 single-state pathway. Four transition structures were found. The first transition state involves the cleavage of the N−O bond of N_2O to create the iron(IV)−oxo species. The high-energy barrier dictates that this step is the rate-determining step of the reaction. Intermediate **B** possesses the iron(IV)−oxo double bond (1.64 Å) with an electronic structure very similar to that found in other nonheme model complexes. The potential energy curve calculated along the Fe−O coordinate predicts that the σ-attack mechanism has a lower energetic requirement than the π-attack mechanism for abstraction of H atom from ethane to form the Fe(III) (S = 5/2)−OH species. Ethanol is formed after the reaction passes from the low-energy barrier of the fourth transition state. The reaction follows a single-state mechanism, as it is dictated by the large energy gaps between the high-spin and intermediate-spin states of all intermediates and transition states. The reaction is highly exothermic with an enthalpy of reaction equal to −146 kJ/mol.

Comparison of the energy barrier of the C−H activation step for methane to that for ethane shows, as expected, that cleaving a C−H bond of ethane is more facile than cleaving a C−H bond of methane. This explains why the MOF, $Fe_{0.1}Mg_{1.9}$(dobdc), catalyzes the hydroxylation of ethane, but methane hydroxylation was not observed. The uncatalyzed reaction is investigated and is found to have an energy barrier of 280 kJ/mol, which clearly implies that the direct reaction between nitrous oxide and ethane is not observable, and iron(IV)−oxo is catalyzing the hydroxylation of ethane to ethanol. Finally, competing pathways were explored, which suggested that hydroxylation is more likely to occur than desaturation and dissociation.

DOI: 10.1021/jacs.5b00382
J. Am. Chem. Soc. 2015, 137, 5770−5781

5. COMPUTATIONAL DETAILS

5.1. Periodic Kohn–Sham Calculations. $Mg_2(dobdc)$[82] (shown in Figure 1) was optimized using periodic boundary conditions with the PBE[83] exchange–correlation functional as implemented in VASP[84] software package. Projector-augmented wave potentials were used to describe the interaction between core and valence electrons. A $2 \times 2 \times 2$ *k*-point integration grid was used with a plane-wave kinetic energy cutoff of 520 eV. Ionic positions were relaxed with energy and force convergence criteria of 10^{-5} eV and 0.05 eV/Å, respectively.

5.2. Kohn–Sham Cluster Calculations. The Gaussian 09 suite of quantum mechanical programs[85] was used for all Kohn–Sham cluster calculations. The density-fitting algorithm was used. The Kohn–Sham determinant was tested for stability and was relaxed to a stable solution using the Stable = Opt keyword of Gaussian. Geometry optimizations were constrained such that all atoms of the MOF portion of the cluster were kept fixed except for the iron atom and the five oxygen atoms composing its first coordination sphere. The atoms of the guest molecules (N_2O, C_2H_6, and their fragments) bound to or reacting with the iron ion of the cluster were always optimized without any constraints. Force constants were determined analytically in the optimized degrees of freedom, and zero-point vibrational energy contributions were added to all energies to produce 0 K enthalpies. The enthalpies at 298.15 K were computed by M06-L/def2-TZVP by adding the zero-point energy and the thermal vibrational-rotaional entropy of the lowest-energy conformer in the quasiharmonic approximation, which corresponds to the harmonic oscillator-rigid rotator approximation with frequencies scaled by a factor of 0.976.[86] The transition structures were characterized by the presence of a single imaginary frequency along the reaction coordinate; all optimized intermediate structures were confirmed to have only real frequencies. Supporting Information also includes single-point calculations on the M06-L/def2-TZVP optimized ground-state geometries performed with def2-TZVPP,[53] cc-pwCVTZ-DK,[87] and cc-pwCVTZ-NR[87] all-electron basis sets to compare relativistic and nonrelativistic effects and to see how the size of the basis set affects our conclusions.

5.3. Conformations. For every structure in Figure 4 except **A**, **E** (which itself is a conformer of **D**), and **TS3** (which is a rotational TS between **D** and **E**), we made an exhaustive search of possible conformations to find the lowest-energy one. Only the results for the lowest-energy ones are presented in the main part of the paper. The complete set of optimized structures is given in Supporting Information.

5.4. Spin Ladder. The Slater determinant of open-shell Kohn–Sham calculations is not an eigenfunction of S^2 (where S is total electron spin) for either the available approximate exchange–correlation functionals or for the unknown exact exchange–correlation functional. We approximated the energies of singlet, triplet, quintet, and septet states by carrying out calculations with spin component M_S equal to 0, 1, 2, and 3, respectively. The spin ladder for the ground-state conformers found in Tables S1–S2 is reported in Table S3 of the Supporting Information. The geometry of the ground-state conformer computed with the quintet spin state was used to perform single-point calculations with M06-L/def2-TZVP for the triplet and singlet spin states. The triplet state was found to be higher in energy than the quintet state by more than 85 kJ/mol for all the intermediates and transition states, and the singlet spin state was found to be higher than the quintet spin state by more than 135 kJ/mol in all cases. These results indicate that the reaction occurs on the quintet surface.

5.5. Multireference Calculations. All multireference calculations were executed with the MOLCAS 7.8 package.[88] Relativistic all-electron basis sets were used for all atoms.[89] In particular, the ANO-RCC-VTZP basis set was used for Fe and the six O atoms that form its first coordination sphere and also for the activated H atom of ethane of **TS2**; the C atoms and the rest of the H atoms of ethane were treated with the ANO-RCC-VDZP basis set, and a minimal basis set (ANO-RCC-MB) was used for all the remaining atoms of the cluster. The mononuclear models were crafted from the M06-L optimized structures of intermediate **B′** (Figure 3) and transition structure **TS2**, and it includes Fe, its first coordination sphere, and some carbon and oxygen atoms of the carboxylic groups; the dangling bonds were saturated with hydrogen atoms, which were optimized with the rest of the atoms fixed; the model has no net charge.

■ ASSOCIATED CONTENT

Ⓢ Supporting Information

Structures and absolute energies in hartrees of all optimized structures. Additional tables and figures. This material is available free of charge via the Internet at http://pubs.acs.org.

■ AUTHOR INFORMATION

Corresponding Authors

*gagliard@umn.edu
*truhlar@umn.edu

Notes

The authors declare no competing financial interest.

■ ACKNOWLEDGMENTS

We thank Larry Que, Xuefei Xu, and Bo Wang for helpful discussions of this work. P.V. acknowledges a Phillips 66 Fellowship for Excellence in Graduate Studies and a Doctoral Dissertation Fellowship. This research was carried out within the Nanoporous Materials Genome Center, which is supported by the U.S. Department of Energy, Office of Basic Energy Sciences, Division of Chemical Sciences, Geosciences, and Biosciences under award DE-FG02-12ER16362.

■ REFERENCES

(1) Nam, W. *Acc. Chem. Res.* **2007**, *40*, 465–465.
(2) Hohenberger, J.; Ray, K.; Meyer, K. *Nat. Commun.* **2012**, *3*, 720.
(3) Groves, J. T. *J. Inorg. Biochem.* **2006**, *100*, 434–447.
(4) Ray, K.; Pfaff, F. F.; Wang, B.; Nam, W. *J. Am. Chem. Soc.* **2014**, *136*, 13942–13958.
(5) Collins, T. J.; Kostka, K. L.; Münck, E.; Uffelman, E. S. *J. Am. Chem. Soc.* **1990**, *112*, 5637–5639.
(6) MacFaul, P. A.; Ingold, K. U.; Wayner, D. D. M.; Que, L., Jr. *J. Am. Chem. Soc.* **1997**, *119*, 10594–10598.
(7) Pestovsky, O.; Stoian, S.; Bominaar, E. L.; Shan, X.; Münck, E.; Que, L., Jr.; Bakac, A. *Angew. Chem., Int. Ed.* **2005**, *44*, 6871–6874.
(8) Bukowski, M. R.; Koehntop, K. D.; Stubna, A.; Bominaar, E. L.; Halfen, J. A.; Münck, E.; Nam, W.; Que, L., Jr. *Science* **2005**, *310*, 1000–1002.
(9) Oliveira, F. T. d.; Chanda, A.; Banerjee, D.; Shan, X.; Mondal, S.; Que, L., Jr.; Bominaar, E. L.; Münck, E.; Collins, T. J. *Science* **2007**, *315*, 835–838.
(10) Lacy, D. C.; Gupta, R.; Stone, K. L.; Greaves, J.; Ziller, J. W.; Hendrich, M. P.; Borovik, A. S. *J. Am. Chem. Soc.* **2010**, *132*, 12188–12190.
(11) Seo, M. S.; Kim, N. H.; Cho, K.-B.; So, J. E.; Park, S. K.; Clémancey, M.; Garcia-Serres, R.; Latour, J.-M.; Shaik, S.; Nam, W. *Chem. Sci.* **2011**, *2*, 1039–1045.
(12) Que, L., Jr. *Acc. Chem. Res.* **2007**, *40*, 493–500.
(13) Nam, W. *Acc. Chem. Res.* **2007**, *40*, 522–531.
(14) Rohde, J.-U.; In, J.-H.; Lim, M. H.; Brennessel, W. W.; Bukowski, M. R.; Stubna, A.; Münck, E.; Nam, W.; Que, L., Jr. *Science* **2003**, *299*, 1037–1039.
(15) Lim, M. H.; Rohde, J.-U.; Stubna, A.; Bukowski, M. R.; Costas, M.; Ho, R. Y. N.; Münck, E.; Nam, W.; Que, L., Jr. *Proc. Natl. Acad. Sci. U.S.A.* **2003**, *100*, 3665–3670.
(16) Price, J. C.; Barr, E. W.; Glass, T. E.; Krebs, C.; Bollinger, J. M., Jr. *J. Am. Chem. Soc.* **2003**, *125*, 13008–13009.
(17) Sinnecker, S.; Svensen, N.; Barr, E. W.; Ye, S.; Bollinger, J. M., Jr.; Neese, F.; Krebs, C. *J. Am. Chem. Soc.* **2007**, *129*, 6168–6179.
(18) Decker, A.; Rohde, J.-U.; Klinker, E. J.; Wong, S. D.; Que, L., Jr.; Solomon, E. I. *J. Am. Chem. Soc.* **2007**, *129*, 15983–15996.

DOI: 10.1021/jacs.5b00382
J. Am. Chem. Soc. 2015, 137, 5770–5781

(19) Solomon, E. I.; Wong, S. D.; Liu, L. V.; Decker, A.; Chow, M. S. *Curr. Opin. Chem. Biol.* **2009**, *13*, 99−113.
(20) Hirao, H.; Kumar, D.; Que, L., Jr.; Shaik, S. *J. Am. Chem. Soc.* **2006**, *128*, 8590−8606.
(21) Ye, S.; Neese, F. *Proc. Natl. Acad. Sci. U.S.A.* **2011**, *108*, 1228−1233.
(22) Grapperhaus, C. A.; Mienert, B.; Bill, E.; Weyhermüller, T.; Wieghardt, K. *Inorg. Chem.* **2000**, *39*, 5306−5317.
(23) Yoon, J.; Wilson, S. A.; Jang, Y. K.; Seo, M. S.; Nehru, K.; Hedman, B.; Hodgson, K. O.; Bill, E.; Solomon, E. I.; Nam, W. *Angew. Chem., Int. Ed.* **2009**, *48*, 1257−1260.
(24) (a) Fang, D.; Lord, R. L.; Cisneros, G. A. *J. Phys. Chem. B* **2013**, *117*, 6410−6420. (b) Fang, D.; Cisneros, G. A. *J. Chem. Theory Comput.* **2014**, *10*, 5136−5148.
(25) Pestovsky, O.; Bakac, A. *J. Am. Chem. Soc.* **2004**, *126*, 13757−13764.
(26) Bernasconi, L.; Louwerse, M. J.; Baerends, E. J. *Eur. J. Inorg. Chem.* **2007**, *2007*, 3023−3033.
(27) England, J.; Martinho, M.; Farquhar, E. R.; Frisch, J. R.; Bominaar, E. L.; Münck, E.; Que, L., Jr. *Angew. Chem., Int. Ed.* **2009**, *48*, 3622−3626.
(28) Cho, K.-B.; Shaik, S.; Nam, W. *Chem. Commun.* **2010**, *46*, 4511−4513.
(29) England, J.; Guo, Y.; Van Heuvelen, K. M.; Cranswick, M. A.; Rohde, G. T.; Bominaar, E. L.; Münck, E.; Que, L., Jr. *J. Am. Chem. Soc.* **2011**, *133*, 11880−11883.
(30) Xiao, D. J.; Bloch, E. D.; Mason, J. A.; Queen, W. L.; Hudson, M. R.; Planas, N.; Borycz, J.; Dzubak, A. L.; Verma, P.; Lee, K.; Bonino, F.; Crocell, V.; Yano, J.; Bordiga, S.; Truhlar, D. G.; Gagliardi, L.; Brown, C. M.; Long, J. R. *Nat. Chem.* **2014**, *6*, 590−595.
(31) Dhuri, S. N.; Seo, M. S.; Lee, Y.-M.; Hirao, H.; Wang, Y.; Nam, W.; Shaik, S. *Angew. Chem., Int. Ed.* **2008**, *47*, 3356−3359.
(32) Hirao, H.; Que, L., Jr.; Nam, W.; Shaik, S. *Chem.—Eur. J.* **2008**, *14*, 1740−1756.
(33) Schröder, D.; Shaik, S.; Schwarz, H. *Acc. Chem. Res.* **2000**, *33*, 139−145.
(34) Shaik, S. *Int. J. Mass spectrom.* **2013**, *354*−*355*, 5−14.
(35) Krebs, C.; Fujimori, D. G.; Walsh, C. T.; Bollinger, J. M. *Acc. Chem. Res.* **2007**, *40*, 484−492.
(36) Price, J. C.; Barr, E. W.; Tirupati, B.; Bollinger, J. M., Jr.; Krebs, C. *Biochemistry* **2003**, *42*, 7497−7508.
(37) Hoffart, L. M.; Barr, E. W.; Guyer, R. B.; Bollinger, J. M., Jr.; Krebs, C. *Proc. Natl. Acad. Sci. U.S.A.* **2006**, *103*, 14738−14743.
(38) Galonić, D. P.; Barr, E. W.; Walsh, C. T.; Bollinger, J. M., Jr.; Krebs, C. *Nat. Chem. Biol.* **2007**, *3*, 113−116.
(39) Eser, B. E.; Barr, E. W.; Frantom, P. A.; Saleh, L.; Bollinger, J. M., Jr.; Krebs, C.; Fitzpatrick, P. F. *J. Am. Chem. Soc.* **2007**, *129*, 11334−11335.
(40) Cho, K.-B.; Wu, X.; Lee, Y.-M.; Kwon, Y.-M.; Shaik, S.; Nam, W. *J. Am. Chem. Soc.* **2012**, *134*, 20222−20225.
(41) Buist, P. H. *Nat. Prod. Rep.* **2004**, *21*, 249−262.
(42) Kumar, D.; de Visser, S. P.; Shaik, S. *J. Am. Chem. Soc.* **2004**, *126*, 5072−5073.
(43) Bigi, M. A.; Reed, S. A.; White, M. C. *Nat. Chem.* **2011**, *3*, 216−222.
(44) (a) Hall, M. B.; Margl, P.; Náray-Szabo, G.; Schramm, V. I.; Truhlar, D. G.; van Santen, R. A.; Warshel, A.; Whitten, J. L. *ACS Symp. Ser.* **1999**, *721*, 2−17. (b) Lonsdale, R.; Ranaghan, K. E.; Mulholland, A. J. *Chem. Commun.* **2010**, *46*, 2354−2372. (c) Cheong, P. H.; Legault, C. Y.; Um, J. M.; Çelebi-Ölçüm, N.; Houk, K. N. *Chem. Rev.* **2011**, *111*, 5042−5137. (d) Bell, A. T.; Head-Gordon, M. *Annu. Rev. Chem. Biomol. Eng.* **2011**, *2*, 453−477.
(45) Usharani, D.; Janardanan, D.; Li, C.; Shaik, S. *Acc. Chem. Res.* **2013**, *46*, 471−482.
(46) Shaik, S.; Chen, H.; Janardanan, D. *Nat. Chem.* **2011**, *3*, 19−27.
(47) Janardanan, D.; Wang, Y.; Schyman, P.; Que, L., Jr.; Shaik, S. *Angew. Chem., Int. Ed.* **2010**, *49*, 3342−3345.
(48) Carter, E. A.; Goddard, W. A. *J. Phys. Chem.* **1988**, *92*, 5679−5683.
(49) Kohn, W.; Becke, A. D.; Parr, R. G. *J. Phys. Chem.* **1996**, *100*, 12974−12980.
(50) Roos, B. O. Multiconfigurational Quantum Chemistry. In *Theory and Applications of Quantum Chemistry: The First Forty Years*; Dykstra, C. E., Frenking, G., Kim, K. S., Scuseria, G. E., Eds.; Elsevier: Amsterdam, 2005; pp 725−764.
(51) Verma, P.; Xu, X.; Truhlar, D. G. *J. Phys. Chem. C* **2013**, *117*, 12648−12660.
(52) Zhao, Y.; Truhlar, D. G. *Theor. Chem. Acc.* **2008**, *120*, 215−241.
(53) (a) Weigend, F.; Ahlrichs, R. *Phys. Chem. Chem. Phys.* **2005**, *7*, 3297−3305. (b) Weigend, F. *Phys. Chem. Chem. Phys.* **2006**, *8*, 1057−1065.
(54) Xu, X.; Truhlar, D. G. *J. Chem. Theory Comput.* **2012**, *8*, 80−90.
(55) Stephens, P. J.; Devlin, F. J.; Chabalowski, C. F.; Frisch, M. J. *J. Phys. Chem.* **1994**, *98*, 11623−11627.
(56) Zhao, Y.; Truhlar, D. G. *Org. Lett.* **2007**, *9*, 1967−1970.
(57) Zhao, Y.; Truhlar, D. G. *J. Chem. Theory Comput.* **2009**, *5*, 324−333.
(58) Kumar, M.; Chaudhari, R. V.; Subramaniam, B.; Jackson, T. A. *Organometallics* **2014**, *33*, 4183−4191.
(59) Liu, Y.; Liu, Y.; Gallo, A. A.; Knierim, K. D.; Taylor, E. R.; Tzeng, N. *J. Mol. Struct.* **2015**, *1084*, 223−228.
(60) Poater, A.; Pump, E.; Vummaleti, S. V. C.; Luigi Cavallo, L. *J. Chem. Theory Comput.* **2014**, *10*, 4442−4448.
(61) Lyngvi, E.; Sanhueza, I. A.; Schoenebeck, F. *Organometallics* **2015**, *34*, 805−812.
(62) Marenich, A. V.; Jerome, S. V.; Cramer, C. J.; Truhlar, D. G. *J. Chem. Theory Comput.* **2012**, *8*, 527−541.
(63) Marenich, A. V.; Cramer, C. J.; Truhlar, D. G. *CM5PAC*; University of Minnesota: Minneapolis, 2011.
(64) Hirshfeld, F. L. *Theor. Chem. Acc.* **1977**, *44*, 129−138.
(65) Glendening, E. D.; Reed, A. E.; Carpenter, J. E.; Weinhold, F. *NBO Version 3.1*; Theoretical Chemistry Institute, University of Wisconsin: Madison, WI, 2013.
(66) (a) Roos, B. O. *Adv. Chem. Phys.* **1987**, *69*, 399−445. (b) Ruedenberg, K.; Cheung, L. M.; Elbert, S. T. *Int. J. Quantum Chem.* **1979**, *16*, 1069−1101.
(67) Srnec, M.; Wong, S. D.; England, J.; Que, L., Jr.; Solomon, E. I. *Proc. Natl. Acad. Sci. U.S.A.* **2012**, *109*, 14326−14331.
(68) Finley, J.; Malmqvist, P.-Å.; Roos, B. O.; Serrano-Andrés, L. *Chem. Phys. Lett.* **1998**, *288*, 299−306.
(69) Bloch, E. D.; Queen, W. L.; Krishna, R.; Zadrozny, J. M.; Brown, C. M.; Long, J. R. *Science* **2012**, *335*, 1606−1610.
(70) Maurice, R.; Verma, P.; Zadrozny, J. M.; Luo, S.; Borycz, J.; Long, J. R.; Truhlar, D. G.; Gagliardi, L. *Inorg. Chem.* **2013**, *52*, 9379−9789.
(71) (a) Yamamoto, A. *Organotransition Metal Chemistry*; Wiley: New York, 1986. (b) Crabtree, R. H. *The Organometallic Chemistry of Transition Metals*; Wiley: New York, 1994.
(72) Shu, L.; Nesheim, J. C.; Kauffmann, K.; Münck, E.; Lipscomb, J. D.; Que, L., Jr. *Science* **1997**, *275*, 515−518.
(73) Andersson, K.; Malmqvist, P.-Å.; Roos, B. O.; Sadlej, A. J.; Wolinski, K. *J. Phys. Chem.* **1990**, *94*, 5483−5488.
(74) Poulos, T. L. *Chem. Rev.* **2014**, *114*, 3919−3962.
(75) Caiyun, G.; Ye, S.; Neese, F. *Angew. Chem., Int. Ed.* **2010**, *49*, 5717−5720.
(76) Janardanan, D.; Usharani, D.; Chen, H.; Shaik, S. *J. Chem. Phys. Lett.* **2011**, *2*, 2610.
(77) Usharani, D.; Janardanan, D.; Shaik, S. *J. Am. Chem. Soc.* **2011**, *133*, 176−179.
(78) Ye, S.; Geng, C.-Y.; Shaik, S.; Neese, F. *Phys. Chem. Chem. Phys.* **2013**, *15*, 8017−8030.
(79) Blanksby, S. J.; Ellison, G. B. *Acc. Chem. Res.* **2003**, *36*, 255−263.
(80) Hammond, G. S. *J. Am. Chem. Soc.* **1955**, *77*, 334−338.
(81) (a) Truhlar, D. G.; Kuppermann, A. *J. Am. Chem. Soc.* **1971**, *93*, 1840−1851. (b) Fukui, K. *Acc. Chem. Res.* **1981**, *14*, 363−368. (c) Hratchian, H. P.; Schlegel, H. B. *J. Chem. Phys.* **2004**, *120*, 9918−9924. (d) Hratchian, H. P.; Schlegel, H. B. *Theory and Applications of Computational Chemistry: The First 40 Years*; Dykstra, C. E., Frenking,

DOI: 10.1021/jacs.5b00382
J. Am. Chem. Soc. 2015, 137, 5770−5781

G., Kim, K. S., Scuseria, G., Eds.; Elsevier: Amsterdam, 2005; pp 195−249. (e) Hratchian, H. P.; Schlegel, H. B. *J. Chem. Theory and Comput.* **2005**, *1*, 61−69.
(82) Queen, W. L.; Brown, C. M.; Britt, D. K.; Zajdel, P.; Hudson, M. R.; Yaghi, O. M. *J. Phys. Chem. C* **2011**, *115*, 24915−24919.
(83) Perdew, J. P.; Burke, K.; Ernzerhof, M. *Phys. Rev. Lett.* **1996**, *77*, 3865−3868.
(84) (a) Kresse, G.; Hafner, J. *Phys. Rev. B* **1993**, *47*, 558−561. (b) Kresse, G.; Hafner, J. *Phys. Rev. B* **1994**, *49*, 14251−14269. (c) Kresse, G.; Furthmüller, J. *Comput. Mater. Sci.* **1996**, *6*, 15−50. (d) Kresse, G.; Furthmüller, J. *Phys. Rev. B* **1996**, *54*, 11169−11186.
(85) Frisch, M. J.; Trucks, G. W.; Schlegel, H. B.; Scuseria, G. E.; Robb, M. A.; Cheeseman, J. R.; Scalmani, G.; Barone, V.; Mennucci, B.; Petersson, G. A.; Nakatsuji, H.; Caricato, M.; Li, X.; Hratchian, H. P.; Izmaylov, A. F.; Bloino, J.; Zheng, G.; Sonnenberg, J. L.; Hada, M.; Ehara, M.; Toyota, K.; Fukuda, R.; Hasegawa, J.; Ishida, M.; Nakajima, T.; Honda, Y.; Kitao, O.; Nakai, H.; Vreven, T.; Montgomery, J. A., Jr.; Peralta, J. E.; Ogliaro, F.; Bearpark, M.; Heyd, J. J.; Brothers, E.; Kudin, K. N.; Staroverov, V. N.; Kobayashi, R.; Normand, J.; Raghavachari, K.; Rendell, A.; Burant, J. C.; Iyengar, S. S.; Tomasi, J.; Cossi, M.; Rega, N.; Millam, J. M.; Klene, M.; Knox, J. E.; Cross, J. B.; Bakken, V.; Adamo, C.; Jaramillo, J.; Gomperts, R.; Stratmann, R. E.; Yazyev, O.; Austin, A. J.; Cammi, R.; Pomelli, C.; Ochterski, J. W.; Martin, R. L.; Morokuma, K.; Zakrzewski, V. G.; Voth, G. A.; Salvador, P.; Dannenberg, J. J.; Dapprich, S.; Daniels, A. D.; Ö. Farkas; Foresman, B.; Ortiz, J. V.; Cioslowski, J.; Fox, D. J. *Gaussian 09*, Revision D.01, Gaussian, Inc.: Wallingford, CT, 2009.
(86) (a) Alecu, I. M.; Zheng, J.; Zhao, Y.; Truhlar, D. G. *J. Chem. Theory Comput.* **2010**, *6*, 2872−2887. (b) http://comp.chem.umn.edu/freqscale/version3b2.htm, accessed Oct. 1, 2014.
(87) Balabanov, N. B.; Peterson, K. A. *J. Chem. Phys.* **2005**, *123*, 064107.
(88) Aquilante, F.; De Vico, L.; Ferré, N.; Ghigo, G.; Malmqvist, P.-Å.; Neogrády, P.; Pedersen, T. B.; Pitonak, M.; Reiher, M.; Roos, B. O.; Serrano-Andrés, L.; Urban, M.; Veryazov, V.; Lindh, R. *J. Comput. Chem.* **2010**, *31*, 224−247.
(89) (a) Roos, B. O.; Lindh, R.; Malmqvist, P.-Å.; Veryazov, V.; Widmark, P.-O. *J. Chem. Phys. A* **2004**, *108*, 2851−2858. (b) Roos, B. O.; Lindh, R.; Malmqvist, P.-Å.; Veryazov, V.; Widmark, P.-O. *J. Chem. Phys. A* **2005**, *109*, 6575−6579.

DOI: 10.1021/jacs.5b00382
J. Am. Chem. Soc. 2015, 137, 5770−5781